J Solid State Electrochem (2011) 15:1833–1843
DOI 10.1007/s10008-011-1364-1

REVIEW

Structure–reactivity relationships in inorganic electrochemistry

Franklin A. Schultz

Received: 17 January 2011 / Revised: 28 February 2011 / Accepted: 28 February 2011 / Published online: 6 April 2011

Abstract Relationships between structure and electron transfer reactivity underlie many important electrochemical applications and provide fundamental insight to chemical and biological processes. The vast array of experimental techniques developed during the latter half of the twentieth century helped greatly to foster progress in this area, and the advent of powerful computational techniques such as density functional theory promises even more far-reaching developments. It is evident that molecular composition, geometric and electronic structure, and changes in these features influence the thermodynamics and kinetics of transition metal electron transfer reactions in predictable and understandable ways. Several examples drawn from the author's research program to illustrate this premise include the influence of sulfur versus oxygen donation on molybdenum-centered electron transfer, reactions in which a change in metal atom spin state accompanies electron transfer, and concomitant multi-electron transfer and metal–metal bond cleavage in binuclear, ligand-bridged complexes.

F. A. Schultz
Department of Chemistry, Indiana University,
800 East Kirkwood Boulevard,
Bloomington, IN 47405, USA

F. A. Schultz (✉)
Department of Chemistry and Chemical Biology,
Indiana University–Purdue University Indianapolis,
402 North Blackford Street,
Indianapolis, IN 46202, USA
e-mail: fschultz@iupui.edu

Introduction

Relationships between structure and electrochemical reactivity underlie the participation of transition metals in many important processes including catalysis, energy conversion, and biological electron transfer. The inherent appeal of the last subject provided an early motivation for the author to undertake molecularly based applications of electrochemistry as a cornerstone of his scientific research. The choice has proved to be a rewarding one because of the intuitively satisfying qualitative picture of electron transfer produced by techniques such as cyclic voltammetry and the ability to achieve a quantitative description of its thermodynamics and kinetics through the application of fundamental principles [1, 2]. The vast array of experimental techniques that were developed and accorded widespread use during the latter half of the twentieth century [3] helped greatly to foster progress in this area. Today, powerful computational methodologies such as digital simulation [4] and density functional theory (DFT) [5] can accurately model the physical and molecular aspects of electron transfer chemistry and promise an even more complete and satisfying picture of structure–reactivity relations.

The current account illustrates several aspects of structure–function correlations in electron transfer chemistry for which a clearer understanding has been reached by electrochemical study. The phenomena investigated include

the influence of coordination environment on the thermodynamics and kinetics of electrochemical reactions, the role of concomitant electronic and geometric structural change in modulating electron transfer, and the discovery of molecular features that promote (often paradoxically so) multi-electron transfer in a single step. Owing to personal taste, many of the systems described feature molybdenum, an element known to be a necessary in biological nitrogen fixation [6, 7] and mammalian metabolic transformations [8, 9]. However, the principles elucidated are applicable to electron transfer reactions in many chemical contexts.

Coordination sphere influences on redox potentials and electron transfer rates—sulfur versus oxygen ligation

Sulfur has long been recognized as a crucial element in the coordination sphere of molybdenum-containing enzymes [10, 11]. It is a prominent component of the catalytic polymetallic $Fe_7S_{8-9}MoX$ cofactor at the active site of nitrogenase [12] and is bound to mononuclear molybdenum centers via pterindithiolate ligands in molybdenum oxo-transferases [13]. Sulfur is thought to facilitate electron transfer to and from the redox-active metal in these biological environments. This supposition has been substantiated through a variety of electrochemical, spectroscopic, and computational model compound studies [14–20] that have clarified the special nature of Mo–S bonding.

Our laboratory began the exploration of sulfur's role by examining the electrochemical behavior of complexes in which oxygen donors are systematically replaced by sulfur [14, 15]. An informative example is provided by the monooxomolybdenum(V) complexes (**1a-c**, **2a-c**; Scheme 1) which contain a tridentate hydrotris(3,5-dimethyl-1-pyrazolyl)borate ligand (Tp*) and a bidentate 1,2-disubstituted aliphatic or aromatic ligand (X-Y) with systematically varied O and S donors. These compounds undergo reduction via the following metal-centered one-electron transfer in non-aqueous media.

$$[Mo^{V}O(Tp^{*})(X-Y)] + e^{-} \leftrightarrows [Mo^{IV}O(Tp^{*})(X-Y)]^{-} \quad E^{o'},\ k_{s,h} \tag{1}$$

Figure 1 and Table 1 demonstrate the dramatic influence of substituting S for O on the thermodynamics and kinetics of reaction 1. The magnitude of the effect is large. Potentials are shifted to more positive values by 750 mV for aliphatic ligands and 600 mV for aromatic ones. Electron transfer kinetics evaluated from the scan rate dependence of the cyclic voltammetric peak potential separation, ΔE_p [21], also illustrate a large influence of coordination environment on rate. As judged from qualitative differences in ΔE_p with

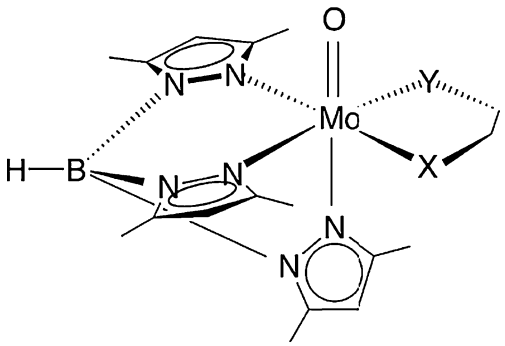

Scheme 1 MoO(Tp*)(X-Y) complexes with X-Y=$^{-}OCH_2CH_2O^{-}$ (**1a**), $^{-}OCH_2CH_2S^{-}$ (**1b**), $^{-}SCH_2CH_2S^{-}$ (**1c**), $^{-}OC_6H_4O^{-}$ (**2a**), $^{-}OC_6H_4S^{-}$ (**2b**), and $^{-}SC_6H_3(CH_3)S^{-}$ (**2c**)

composition (Fig. 1), much slower electron transfer kinetics prevail at oxygen-coordinated centers. Indeed, measurements at ambient temperature (298 K) reveal an approximate 30-fold enhancement in $k_{s,h}$ for compound **1c** over **1a** and a 10-fold enhancement for **2c** over **2a** (Table 1). Faster rates also are observed for complexes with aromatic rather than aliphatic ligand skeletons.

We recently determined the electrochemical activation parameters of reaction 1 to provide a more complete description of the molecular features governing electron transfer rates. Temperature-dependent measurements of $k_{s,h}$ based on the classical Marcus theory, Eq. 2 [22, 23], were conducted to obtain values of $\Delta H_{obs}^{\ddagger}$ and A_{het} as shown in Table 1.

$$k_{s,h} = A_{het} \cdot \exp\left[-\Delta H^{\ddagger}_{obs}/RT\right] \tag{2}$$

The trends in $\Delta H_{obs}^{\ddagger}$ are generally in accord with the ambient temperature rate constants. The enthalpies of activation are largest for aliphatic oxygen-ligated complexes and smallest for aromatic sulfur-ligated ones. $\Delta H_{obs}^{\ddagger}$

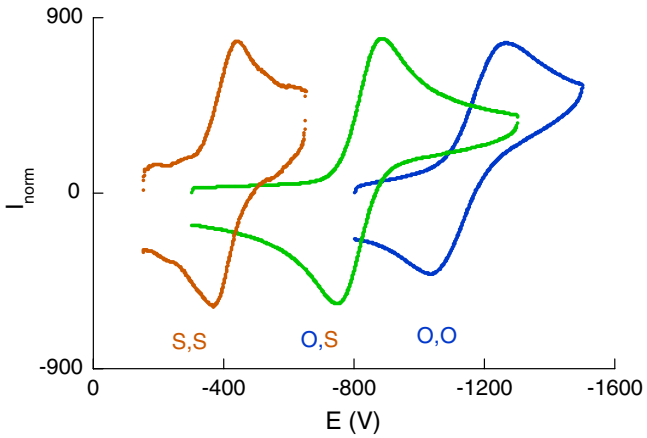

Fig. 1 Current-normalized cyclic voltammograms of **1a** (*blue*), **1b** (*green*), and **1c** (*orange*) in 0.3 M Bu_4NPF_6/CH_3CN at a scan rate of 5 Vs^{-1}. Pt working electrode; Ag/AgCl reference electrode

Table 1 Electrochemical data for reduction of oxygen- and sulfur-ligated oxomolydbenum (V) complexes in 0.3 M Bu_4NPF_6/CH_3CN

Complex	Bidentate ligand donors	$E^{\circ\prime}_{298}$ (V versus Ag/AgCl)	$k_{s,h}^{298}$ (cm s^{-1})	$\Delta H_{obs}^{\ddagger}$ (kJ mol^{-1})	$\Delta H^{\ddagger}_{is}$[a] (kJ mol^{-1})	A_{het} (cm s^{-1})
1a	O,O	−1.145	7.7×10^{-3}	36	17	1.3×10^{4}
1b	O,S	−0.813	2.8×10^{-2}	35	16	4.4×10^{4}
1c	S,S	−0.402	2.4×10^{-1}	27	8	1.2×10^{4}
2a	O,O	−0.721	2.6×10^{-2}	23	8	2.5×10^{2}
2b	O,S	−0.445	1.6×10^{-1}	14	−1	0.5×10^{2}
2c	S,S	−0.112	3.1×10^{-1}	13	−2	0.5×10^{2}

Data for reduction of oxygen- and sulfur-ligated oxomolydbenum(V) complexes in 0.3 M Bu_4NPF_6/CH_3CN from [15]

[a] Calculated from $\Delta H_{obs}^{\ddagger}$ as described in the text

decreases by 9–10 kJ mol^{-1} on passing from complexes with two O donors to ones with two S donors for both aliphatic and aromatic ligands. To obtain the inner shell contribution to the enthalpy of activation, an outer shell contribution of $\Delta H_{os}^{\ddagger}$=19 kJ mol^{-1} for compounds **1a–1c** and 15 kJ mol^{-1} for compounds **2a–2c** was estimated [15] and subtracted from the total barrier height to yield $\Delta H_{is}^{\ddagger}=\Delta H_{obs}^{\ddagger}-\Delta H_{os}^{\ddagger}$. Inspection of $\Delta H_{is}^{\ddagger}$ values in Table 1 reveals that inner shell reorganization is the principal factor responsible for the observation of slower electron transfer kinetics in O- versus S-ligated species and in complexes with aliphatic versus aromatic ligands. Although variations in the experimentally determined pre-exponential factor are counter to this trend (A_{het} is 50–200 times larger for aliphatic versus aromatic X-Y ligands, but is uninfluenced by the nature of the donor atom), the small differences in A_{het} do not obscure the influence of donor atom on electrode kinetics.

Ligand control of metal-centered redox potentials frequently is interpreted in terms of a ligand field model [24] wherein the electron donating and withdrawing properties of ligand constituents modulate the energy of the redox-active orbital—in this case the non-bonding metal-centered Mo d_{xy} orbital. The results in Table 1 are consistent with this interpretation as well as the intuitive expectation from hard and soft acid–base theory [25] that O versus S donors and aliphatic versus aromatic frameworks are more effective negative charge donors to metal centers. However, more fundamental explanations appear to underlie the pronounced impact of S for O substitution on redox behavior. This is particularly so upon considering the influence of donor atom on rate. If a simple harmonic oscillator model is assumed for nuclear reorganization [14], metal–ligand bond elongations of 0.08–0.18 Å are required to produce a 10-kJ mol^{-1} difference in inner shell barrier height between O,O- and S,S-coordinated centers. Bond distance changes of this magnitude are unreasonably large for electron transfer involving a non-bonding redox orbital, which begs a more fundamental interpretation of results.

The most satisfying explanation of our observations derives from spectroscopic studies of oxomolybdenum-1,2-dithiolene complexes [20, 26] which reveal the presence of a highly covalent interaction between the in-plane S donor orbitals and the Mo d_{xy} redox orbital. This overlap provides an effective pathway for intramolecular charge redistribution (electronic relaxation) in conjunction with electron transfer. Experimental and computational studies of related metal–sulfur systems [27–29] have ascertained that the greater intramolecular electronic relaxation available through metal–sulfur covalency dramatically influences the thermodynamics and kinetics of metal-centered electron transfer in comparison with other ligand environments. Because nuclear and electronic distortions generally are coupled, the experimentally more evident nuclear structural changes traditionally have been viewed as controlling electron transfer behavior, as found, for example, in the simple harmonic oscillator model of electron transfer-induced nuclear reorganization. However, electronic structural differences inherently are more energetic and can override the contributions from purely nuclear reorganization. Further theoretical studies should provide a better understanding of the influence of electronic structural relaxation on the thermodynamics and kinetics of electron transfer reactions.

The role of electronic structure—coupled electron transfer and spin crossover

Reactions in which electron transfer is coupled to a change in metal–atom spin state [30] are of widespread importance. Examples of such processes are found in the regulation of biological function [31], chemical catalysis [32], and molecular device operation [33, 34]. Moreover, the mechanism of coupled electron transfer and spin crossover, as occurs in LS-Co(III) (t_{2g}^{6}) to HS-Co(II) ($t_{2g}^{5}e_{g}^{2}$) reduction, has been of long-standing fundamental interest in inorganic chemistry [35–37].

We became interested in this subject while studying the electrochemical behavior of a series of metal–bis (1,4,7-triazacyclononane) (tacn) complexes [38]. These M $(tacn)_2^{3+/2+}$ (M = Fe, Co, Ni, Ru) couples exhibit heterogeneous electron transfer rates that accord with the predictions of Marcus theory, i.e., $k_{s,h}$ decreases systematically as the extent of electron transfer-induced metal–ligand bond elongation increases. However, the $Fe(tacn)_2^{3+/2+}$ and $Co(tacn)_2^{3+/2+}$ half-reactions, which are characterized by a change in metal–atom spin state, exhibit highly unusual activation parameters ($\Delta H_{obs}^{\ddagger}$, A_{het}). This observation motivated us to undertake more comprehensive studies of several $M(tacn)_2^{3+/2+}$ and $M(pzb)_2^{+/0}$ [pzb^-=hydrotris(pyrazolyl)borate (Tp), tetrakis(pyrazolyl)borate (pzTp), or hydrotris(3,5-dimethylpyrazolyl)borate (Tp*)] redox systems (Eqs. 3 and 4) to better understand the influence of spin crossover on electron transfer behavior.

$$M(tacn)_2^{3+} + e^- \leftrightarrows M(tacn)_2^{2+} \quad E^{\circ\prime}_{obs}, \quad (k_{s,h})_{obs} \tag{3}$$

$$M(pzb)_2^{+} + e^- \leftrightarrows M(pzb)_2^{0} \quad E^{\circ\prime}_{obs}, \quad (k_{s,h})_{obs} \tag{4}$$

Octahedral complexes of first row transition metals having d^4 through d^7 electronic configurations can exist in more than one spin state. Low-spin (LS) forms are favored by strong ligand fields and high oxidation states; high-spin (HS) forms are favored by weak ligand fields and low oxidation states. Spin crossover also leads to significant structural change as a result of the change in occupancy of the metal–ligand antibonding orbitals. For example, LS-Fe(II) (t_{2g}^6)→HS-Fe (II) $(t_{2g}^4e_g^2)$ conversion in FeN_6 complexes leads to an increase of ~0.2 Å in the average Fe–N distance [39].

Coupled electrochemical and spin crossover reactions are interpreted in terms of the square scheme shown in Scheme 2. $E^{\circ\prime}_{LS}$ and $E^{\circ\prime}_{HS}$ and $(k_{s,h})_{LS}$ and $(k_{s,h})_{HS}$ are the $M^{3+/2+}$ potentials and electron transfer rate constants of the individual spin states, and $K_{se,2+}$ and $K_{se,3+}$ are the equilibrium constants for LS⇌HS conversion. Typically, $K_{se,2+} > K_{se,3+}$ and $E^{\circ\prime}_{HS} > E^{\circ\prime}_{LS}$ because the higher oxidation state usually exhibits a greater ligand field strength. Electrode potentials and spin equilibrium constants in Scheme 2 are related by Eq. 5.

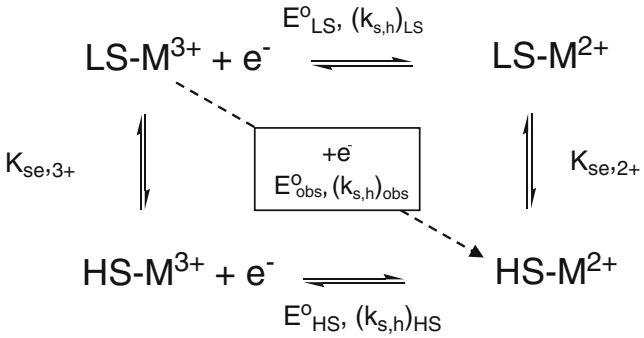

Scheme 2 Electrochemical square scheme for coupled electron transfer and spin crossover reactions

$$E^{\circ\prime}_{HS} - E^{\circ\prime}_{LS} = (RT/F)\ \ln\left(K_{se,2+}/K_{se,3+}\right) \tag{5}$$

The observed potential for spin crossover-coupled electron transfer, $E^{\circ\prime}_{obs}$, is given by Eq. 6a or 6b.

$$E^{\circ\prime}_{obs} = E^{\circ\prime}_{LS} + (RT/F)\ \ln\left[\left(1+K_{se,2+}\right)/\left(1+K_{se,3+}\right)\right] \tag{6a}$$

$$E^{\circ\prime}_{obs} = E^{\circ\prime}_{HS} + (RT/F)\ \ln\left[K_{se,3+}\left(1+K_{se,2+}\right)/K_{se,2+}\left(1+K_{se,3+}\right)\right] \tag{6b}$$

Because spin crossover generally is observed in only one of the two available oxidation states, Eqs. 6a and 6b may be simplified to Eqs. 7a and 7b using $x_{LS,2+}$ and $x_{HS,3+}$ to represent the mole fractions of the LS and HS forms in the relevant oxidation states.

$$\begin{aligned} E^{\circ\prime}_{obs} &\cong E^{\circ\prime}_{LS} + (RT/F)\ \ln\left(1+K_{se,2+}\right) \\ &= E^{\circ\prime}_{LS} - (RT/F)\ \ln\left(x_{LS,2+}\right) \end{aligned} \tag{7a}$$

$$\begin{aligned} E^{\circ\prime}_{obs} &\cong E^{\circ\prime}_{HS} + (RT/F)\ \ln\left[K_{se,3+}/\left(1+K_{se,3+}\right)\right] \\ &= E^{\circ\prime}_{HS} + (RT/F)\ln\left(x_{HS,3+}\right) \end{aligned} \tag{7b}$$

We have determined that $K_{se,2+}$=0.25 for the $LS\text{-}Fe(tacn)_2^{2+} \rightleftharpoons HS\text{-}Fe(tacn)_2^{2+}$ equilibrium at 298 K in D_2O [40] and have confirmed the validity of the above interpretation by extracting the intrinsic $E^{\circ\prime}_{LS}$ value for $Fe(tacn)_2^{3+/2+}$ reduction from temperature-dependent measurements of $K_{se,2+}$ and $E^{\circ\prime}_{obs}$ [41].

Solution phase spin equilibria for the remaining metal–bis(tacn) complexes are not observable at experimentally accessible temperatures. Consequently, we have pursued a computational approach to more fully understand periodic trends in redox potentials and spin crossover behavior for these first row transition metal complexes [42]. Density functional theory is a firmly established method for computing redox potentials with a benchmark accuracy of ~150 mV [43]. Application of DFT to spin-state calculations is more problematic [44], but the methodology is becoming more widely applied for this purpose and its semi-quantitative reliability has been established through a variety of studies [42, 45–49].

Computed values of $K_{se,2+}$, $K_{se,3+}$, $E^{\circ\prime}_{HS}$, and $E^{\circ\prime}_{LS}$ and the value $E^{\circ\prime}_{comp}$ calculated by means of Eqs. 6a and 6b are presented in Table 2. Agreement between $E^{\circ\prime}_{comp}$ and $E^{\circ\prime}_{obs}$

Table 2 Comparison of experimental and computed electrode potentials (V versus NHE) and spin equilibrium constants for $M(tacn)_2^{3+/2+}$ redox systems in H_2O at 298 K

Half-reaction	$K_{se,2+}$ [a]	$K_{se,3+}$ [a]	$E^{\circ\prime}_{HS}$ [a]	$E^{\circ\prime}_{LS}$ [a]	$E^{\circ\prime}_{comp}$ [b]	$E^{\circ\prime}_{obs}$
$Cr(tacn)_2^{3+}+e^- \leftrightarrows Cr(tacn)_2^{2+}$	2.9×10^{9}	–	−0.99	−1.55	−0.99	−1.14[d]
$Mn(tacn)_2^{3+}+e^- \leftrightarrows Mn(tacn)_2^{2+}$	3.2×10^{28}	3.2×10^{1}	+0.46	−1.02	+0.46	+0.62[d,e]
$Fe(tacn)_2^{3+}+e^- \leftrightarrows Fe(tacn)_2^{2+}$	3.4×10^{-1} (2.5×10^{-1})[c]	2.3×10^{-8}	+0.55	+0.13	+0.14	+0.13[f]
$Co(tacn)_2^{3+}+e^- \leftrightarrows Co(tacn)_2^{2+}$	1.5×10^{1}	9.3×10^{-33}	+1.51	−0.46	−0.38	−0.40[f]
$Ni(tacn)_2^{3+}+e^- \leftrightarrows Ni(tacn)_2^{2+}$	–	5.5×10^{-23}	+2.29	+0.97	+0.97	+0.95[f]

[a] Computed by density functional theory as described in [42]

[b] Calculated by use of Eq. 6a or 6b

[c] Experimental result in D_2O from [40]

[d] From [50]

[e] Estimated from data at 276 K

[f] Ion pair-corrected data from [38]

and between the calculated and experimental value of $K_{se,2+}$ for $Fe(tacn)_2^{2+}$ spin crossover is excellent. The high accuracy of these results may be fortuitous given the limitations of DFT in dealing with open-shell systems. However, the results in Table 2 clearly demonstrate the influence of spin state on redox thermodynamics. As anticipated on an intuitive basis, LS→HS conversion is favored to a much greater extent in M^{2+} versus M^{3+} oxidation states, and $E^{\circ\prime}_{HS}$ values are much more positive than $E^{\circ\prime}_{LS}$. The range of $E^{\circ\prime}_{HS}-E^{\circ\prime}_{LS}$ differences is remarkably large, 0.4–2.0 V. Extreme values of $K_{se,2+}$ and $K_{se,3+}$ identify high-energy spin-state forms (LS-Mn^{2+}, HS-Co^{3+}, HS-Ni^{3+}) that likely are avoided in redox transformations. Intermediate values of $K_{se,2+}$ and $K_{se,3+}$ indicate forms (LS-Cr^{2+}, HS-Fe^{3+}) that are conceivably attainable. Values of $K_{se,3+}$ or $K_{se,2+}\approx1$ for Mn^{3+}, Co^{2+}, and Fe^{2+} suggest that multiple spin-state forms should be accessible in these oxidation states, although LS⇌HS equilibrium has been observed only for $Fe(tacn)_2^{2+}$.

Plots of $E^{\circ\prime}_{comp}$ and $E^{\circ\prime}_{obs}$ versus atomic number for the $M(tacn)_2^{3+/2+}$ couples are shown in Fig. 2. The non-periodic "sawtooth" pattern found there commonly is observed for first row redox systems [51]. However, this behavior contrasts with the expectation that electron attachment energies will become increasingly favorable with increasing nuclear charge, as is true for bare metal ions [52, 53]. The spin-state energies presented in Table 2 provide a definitive explanation for the deviation from monotonic behavior. Specifically, destabilization of the LS-Mn(II) and HS-Co(III) states drives the potentials of the $Mn(tacn)_2^{3+/2+}$ and $Co(tacn)_2^{3+/2+}$ couples to values that, respectively, are far above and far below the response expected for a systematic increase in $E^{\circ\prime}$ with atomic number. Spin-state energetics presumably account for a similar sawtooth progression in $E^{\circ\prime}$ for $M(Tp)_2^{+/0}$ couples (Fig. 2, gray line), although computations have not been completed for this family of compounds.

It has been known for some time that electron transfer reactions accompanied by a spin-state change are slow [55]. This is amply demonstrated in Fig. 3 where oxidation of $Mn(Tp^*)_2$ exhibits a large cyclic voltammetric peak potential separation and the subsequent oxidation of $Mn(Tp^*)_2^+$ does not. The $Mn(Tp^*)_2^+$ intermediate is an unusual example of a low-spin Mn(III) complex. This property has been confirmed by isolation and magnetic, spectroscopic, and X-ray structural characterization of three $[Mn(pzb)_2]SbF_6$ (pzb^-=$pzTp^-$, Tp^- or Tp^{*-}) salts [56]. Electrochemical oxidation of $Mn(pzb)_2$ complexes there-

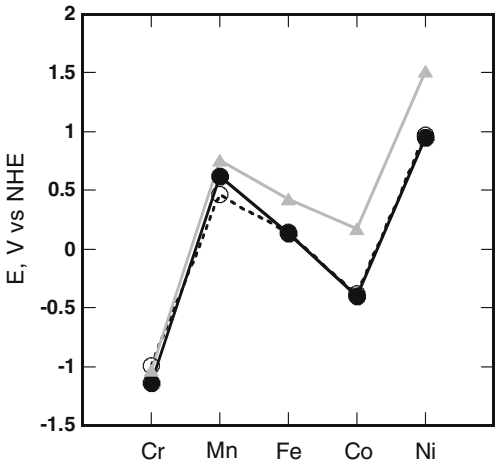

Fig. 2 $MN_6^{3+/2+}$ redox potentials for first row transition metals: experimental values (*filled circles*, *solid line*) and computed values (*open circles*, *dashed line*) for $M(tacn)_2^{3+/2+}$ in water; experimental values for $M(Tp)_2^{+/0}$ (*filled triangles*, *gray line*) in 1,2-dichloroethane from [54]

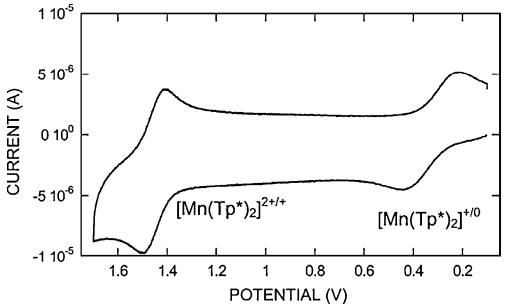

Fig. 3 Cyclic voltammetric oxidation of 2.4×10^{-4} M $Mn(Tp^*)_2$ in 1,2-dichloroethane containing 0.1 M Bu_4NPF_6. Scan rate=0.1 Vs^{-1}; Ag/AgCl reference electrode (reprinted with permission from [54], Copyright 2003, American Chemical Society)

fore is concluded to proceed according to a reaction that is accompanied by a spin-state change:

$$HS-Mn^{II}(pzb)_2{}^0\left(t_{2g}{}^3e_g{}^2\right)\leftrightarrows\ LS-Mn^{III}(pzb)_2{}^+\left(t_{2g}{}^4\right)+e^- \quad (8)$$

and to be followed by one that is not:

$$LS-Mn^{III}(pzb)_2{}^+\left(t_{2g}{}^4\right)\overleftrightarrows\ Mn^{IV}(pzb)_2{}^{2+}\left(t_{2g}{}^3\right)+e^- \quad (9)$$

In accord with this interpretation, peak potential separations are larger and $(k_{s,h})_{obs}$ values are 10–100 times smaller for reaction 8 in comparison with reaction 9 [56].

Values of $(k_{s,h})_{obs}$ determined for four $M(tacn)_2{}^{3+/2+}$ couples and nine $M(pzb)_2{}^{+/0}$ couples are collected in Table 3. It is evident that electrode reactions accompanied by a complete change in spin state exhibit the smallest values of $(k_{s,h})_{obs}$. The difference is particularly noticeable for $Co^{3+/2+}$ and $Mn^{3+/2+}$ couples where the number of antibonding electrons increases by 2 upon reduction. For $M(pzb)_2{}^{+/0}$ complexes, the position of LS⇌HS equilibrium can be altered by changing the pattern of ligand substitution [57]. As an example, $Fe(pzTp)_2$ is fully LS, $Fe(Tp^*)_2$ is fully HS, and $Fe(Tp)_2$ exhibits a spin equilibrium with K_{se}= 0.078 at 263 K [58]. Accordingly, heterogeneous electron transfer rates for reduction of low-spin $Fe(pzb)_2{}^+$ decrease in the sequence pzTp≈Tp>Tp*. As shown in Fig. 4, the trend pzTp>Tp>Tp* is dramatically evident from the peak potential separations of $Co(pzb)_2{}^{+/0}$ couples. Here, the Co (II) state is fully HS in all three cases. In contrast, the sequence changes to Tp*>pzTp>Tp for $Mn(pzb)_2{}^{+/0}$ (Table 3). In this case, the smaller HS-LS energy gap is found in the higher oxidation state (Table 2), which suggests that $Mn(pzb)_2{}^+$ spin crossover modulates the observed electron transfer rate.

The mechanism of coupled electron transfer and spin crossover has been a long debated topic in inorganic chemistry [30, 35–37]. A LS-M^{3+}+e^-→HS-M^{2+} reaction must proceed either through a high-energy spin-state intermediate (LS-M^{2+} or HS-M^{3+}) or in a concerted manner (i.e., via a path with a single transition state) diagonally across the square (Scheme 2, dashed line). In an effort to answer this question, we determined activation parameters for the $M(tacn)_2{}^{3+/2+}$ and $Fe(pzb)_2{}^{+/0}$ redox couples by temperature-dependent measurement of $(k_{s,h})_{obs}$ and

Table 3 Heterogeneous electron transfer rate constants and enthalpies of activation for $M(tacn)_2{}^{3+/2+}$ and $M(pzb)_2{}^{+/0}$ redox couples

Redox couple	$(k_{s,h})_{obs}$ (cm s^{-1})	$\Delta H^{\ddagger}_{obs}$ [a] (kJ mol^{-1})	$\Delta H^{\ddagger}_{is}$ [b] (kJ mol^{-1})
LS-$Ru(tacn)_2{}^{3+}$+e^-⇆LS-$Ru(tacn)_2{}^{2+}$ [c]	1.3×10^{0}	16	1
LS-$Fe(tacn)_2{}^{3+}$+e^-⇆LS/HS-$Fe(tacn)_2{}^{2+}$[c]	8.0×10^{-1}	22	7
LS-$Ni(tacn)_2{}^{3+}$+e^-⇆$Ni(tacn)_2{}^{2+}$[c]	1.2×10^{-1}	23	8
LS-$Co(tacn)_2{}^{3+}$ + e^- ⇆ HS-$Co(tacn)_2{}^{2+}$[c]	1.6×10^{-2}	70	55
LS-$Mn(pzTp)_2{}^{+}$+e^-⇆HS-$Mn(pzTp)_2{}^{0}$[d]	7.8×10^{-4}		
LS-$Mn(Tp)_2{}^{+}$+e^-⇆HS-$Mn(Tp)_2{}^{0}$[d]	1.8×10^{-4}		
LS-$Mn(Tp^*)_2{}^{+}$+e^-⇆HS-$Mn(Tp^*)_2{}^{0}$[d]	2.6×10^{-3}		
LS-$Fe(pzTp)_2{}^{+}$+e^-⇆LS-$Fe(pzTp)_2{}^{0}$[e]	1.5×10^{0}	20	5
LS-$Fe(Tp)_2{}^{+}$+e^-⇆LS/HS-$Fe(Tp)_2{}^{0}$[e]	2.2×10^{0}	15	0
LS-$Fe(Tp^*)_2{}^{+}$+e^-⇆HS-$Fe(Tp^*)_2{}^{0}$[e]	9.0×10^{-2}	30	15
LS-$Co(pzTp)_2{}^{+}$+e^-⇆HS-$Co(pzTp)_2{}^{0}$[f]	4.4×10^{-3}		
LS-$Co(Tp)_2{}^{+}$+e^-⇆HS-$Co(Tp)_2{}^{0}$[f]	1.9×10^{-4}		
LS-$Co(Tp^*)_2{}^{+}$+e^-⇆HS-$Co(Tp^*)_2{}^{0}$[f]	2.2×10^{-5}		

[a] Determined from the temperature dependence of $(k_{s,h})_{obs}$

[b] Determined as $\Delta H_{is}^{\ddagger}=\Delta H_{obs}^{\ddagger}-\Delta H_{os}^{\ddagger}$, assuming $\Delta H_{os}^{\ddagger}$=15 kJ mol^{-1}

[c] In aqueous NaF electrolyte and corrected for electrical double layer effects from [38]

[d] In 0.1 M Bu_4NPF_6/CH_3CN from [56]

[e] In 0.3 M Bu_4NPF_6/CH_3CN from [58]

[f] In 0.1 M Bu_4NPF_6/1,2-dichloroethane from [54]

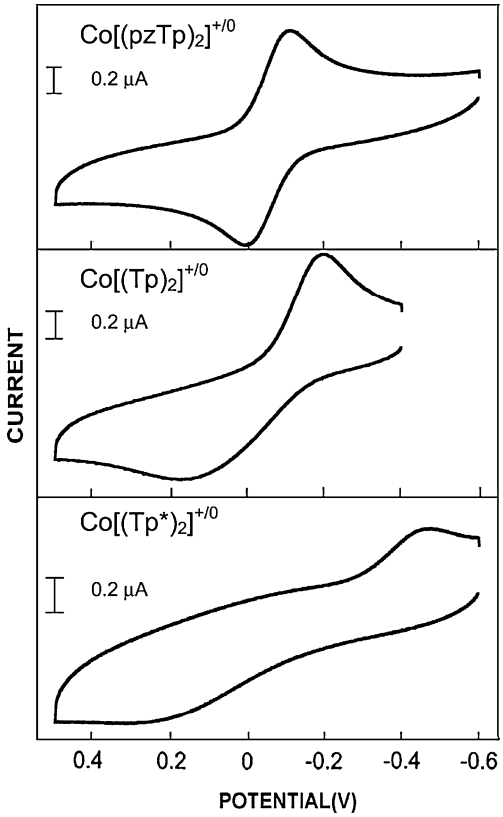

Fig. 4 Cyclic voltammetric oxidation of 3.5×10^{-4} M $Co(pzTp)_2$ (*top*), 3.0×10^{-4} M $Co(Tp)_2$ (*middle*), and 5.3×10^{-4} M $Co(Tp^*)_2$ (*bottom*) in 1,2-dichloroethane containing 0.1 M Bu_4NPF_6. Scan rate= 0.1 Vs^{-1}; Ag/AgCl reference electrode (reprinted with permission from [54], Copyright 2003, American Chemical Society)

extracted the inner shell portion of the enthalpy of activation enthalpy, $\Delta H_{is}^{\ddagger}$, by subtracting an outer shell contribution from $\Delta H_{obs}^{\ddagger}$ (Table 3). Unusually large inner shell barriers are observed for the $Co(tacn)_2^{3+/2+}$ and $Fe(Tp^*)_2^{+/0}$ reactions, which occur with complete spin-state conversion. Larger than anticipated inner shell barriers are consistent with reduction via a "HS pathway," which proceeds by chemical conversion of LS-M^{3+} to HS-M^{3+} followed by electron transfer, i.e., along the left-hand side and bottom of Scheme 2 [58]. However, this conclusion contrasts with the observation (Table 2) that LS-M^{2+} rather than HS-M^{3+} states are energetically more accessible for these redox systems. Thus, temperature-dependent electrochemical measurements have neither answered the question of mechanism nor established whether spin crossover-coupled electron transfer occurs in a concerted or stepwise manner. Further studies thus are needed to decide among the mechanistic possibilities.

Structurally induced multi-electron transfer

Multi-electron transfer reactions occur widely in chemistry and biology and are crucial to many small-molecule activation processes. One-step multi-electron transfer is at first glance paradoxical because addition of a second unit of charge should be electrostatically more difficult than addition of a first. However, compositional changes accompanying electron transfer can compensate for the unfavorable energetics of charge addition and produce a multi-electron event by inversion of the one-electron potentials [59]. Many multi-electron examples having this characteristic have been reported, including reactions where electron transfer is accompanied by proton transfer [60]:

$$Os^{VI}O(OH)(OH_2)(trpy)^{3+} + 3H^+ + 3e^- \leftrightarrows Os^{III}(OH_2)_3(trpy)^{3+} \quad (10)$$

or by a change in coordination number [61]:

$$Mo^{VI}O(S_2CNEt_2)_3^+ + 2e^- \leftrightarrows Mo^{IV}O(S_2CNEt_2)_2 + Et_2NCS_2^- \quad (11)$$

Some years ago, we encountered a perplexing example wherein binuclear ligand-bridged molybdenum and tungsten carbonyls appeared to undergo two-electron transfer in a single step without a change in composition (Scheme 3) [62–64]. The two-electron nature of the $[M_2(\mu\text{-}ER_n)_2(CO)_8]^{0/2-}$ transformations was supported by the peak potential separations and current magnitudes of their voltammetric traces relative to those of one-electron systems (Fig. 5). Isolation and structural characterization of a number of neutral and dianionic reactants [65, 66] confirmed this observation, but the question remained: "How does multi-electron transfer occur?"

An outward explanation is that $M(I)_2$ to $M(0)_2$ dimer reduction is accompanied by cleavage of a metal–metal single bond and significant structural rearrangement within the $M_2(ER_n)_2$ core. Indeed, increases of ~1 Å in the M–M bond distance and ~30° in the M–E–M bridge angle occur

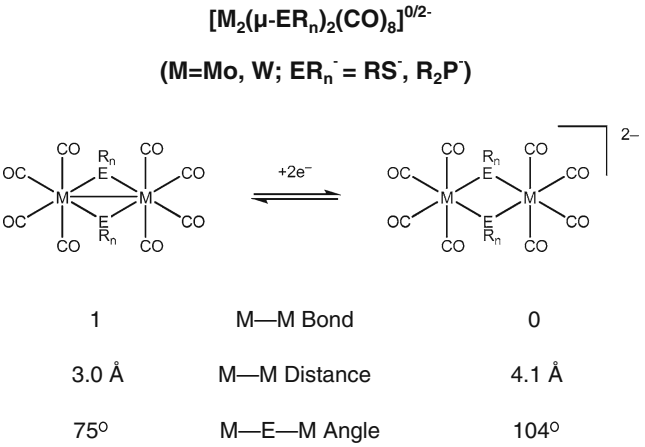

Scheme 3 Structural changes accompanying two-electron transfer in $[M_2(\mu\text{-}ER_n)_2(CO)_8]^{0/2-}$ redox systems

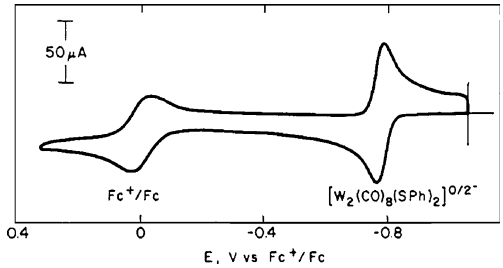

Fig. 5 Cyclic voltammetric trace for oxidation of equal concentrations of $(Bu_4N)_2[W_2(\mu\text{-}SPh)_2(CO)_8]$ and ferrocene at 0.1 V s^{-1} in *N*,*N*-dimethylformamide (reprinted with permission from [62], Copyright 1986, American Chemical Society)

upon two-electron reduction of the oxidized species to its dianion (Scheme 3). These structural changes are thought to provide the driving force for inversion of the one-electron $M_2(\mu\text{-}ER_n)_2(CO)_8$ potentials. This interpretation is supported by extended Hückel molecular orbital calculations of ligand-bridged dimeric systems (Fig. 6) [67, 68] which show that the energy of the redox-active σ^* metal–metal antibonding orbital decreases dramatically in concert with the electron transfer-induced M–E–M bridge angle opening and M–M bond lengthening.

Using electron transfer-induced structural change as an interpretive framework, we employed electrochemical theory for two-electron electrode reactions [69] to resolve the thermodynamics and kinetics of $M_2(\mu\text{-}ER_n)_2(CO)_8$ reduction [68].

$$M_2(\mu\text{-}ER_n)_2(CO)_8 + e^- \leftrightarrows M_2(\mu\text{-}ER_n)_2(CO)_8^- \qquad E_i^{\circ\prime},\ \alpha_i,\ k_{sh,i} \tag{12a}$$

$$M_2(\mu\text{-}ER_n)_2(CO)_8^- + e^- \leftrightarrows M_2(\mu\text{-}ER_n)_2(CO)_8^{2-} \qquad E_{ii}^{\circ\prime},\ \alpha_{ii},\ k_{sh,ii} \tag{12b}$$

Table 4 contains comparative data for several of these redox systems. It is not possible to isolate the individual one-electron steps as discrete voltammetric waves. Moreover, the electron transfer kinetics of the sulfido-bridged derivatives are so facile that only lower limits to k_{sh} and $\Delta E^{\circ\prime}$ can be obtained. However, electron transfer is more sluggish for the phosphido-bridged compounds, which allows reaction 12b to be identified as the rate-limiting step and the charge transfer kinetics and the extent of potential inversion to be deconvoluted quantitatively from the experimental data.

Several important conclusions are evident from the experimental $E^{\circ\prime}$ and k_{sh} values in Table 4. (1) Potential inversion occurs in both the $[M_2(\mu\text{-}SR)_2(CO)_8]^{0/2-}$ and $[M_2(\mu\text{-}PR_2)_2(CO)_8]^{0/2-}$ redox systems, a finding that is consistent with the one-step, two-electron reactions of these compounds. The extent of potential inversion is greater for phosphido-bridged complexes, being approx. +180 mV versus approx. +20 mV for their sulfido-bridged analogs. (2) Values of $E_i^{\circ\prime}$, $E_{ii}^{\circ\prime}$, and $E_{mid}^{\circ\prime}$ are virtually metal-independent, but are approx. 0.5 V more negative for R_2P^--versus RS^--bridged species, which suggests that the

Table 4 Experimental and computed data for two-electron reduction of selected $[M_2(\mu\text{-}ER_n)_2(CO)_8]^{0/2-}$ complexes

$M_2(\mu\text{-}ER_n)_2$	Experiment						Computation[a]			
	$E_i^{\circ\prime}$ (V)	$E_{ii}^{\circ\prime}$ (V)	$E_{mid}^{\circ\prime}$ (V)	$\Delta E^{\circ\prime}$ (mV)	$k_{sh,i}$ (cm s^{-1})	$k_{sh,ii}$ (cm s^{-1})	$E_{i,comp}^{\circ\prime}$ (V)	$E_{ii,comp}^{\circ\prime}$ (V)	$E_{mid,comp}^{\circ\prime}$ (V)	$\Delta E_{comp}^{\circ\prime}$ (mV)
$Mo_2(SPh)_2$[b]	–	–	−0.79	–	–	–	−0.63	−0.64	−0.63	−10
$W_2(SPh)_2$[b]	–	–	−0.80	+20[d]	$\geq 1.0\times10^{-1}$ [d]	$\geq 1.0\times10^{-1}$ [d]	−0.65	−0.63	−0.64	+20
$Mo_2(PPh_2)_2$[c]	−1.45	−1.28	−1.36	+170	4.0×10^{-1}	3.8×10^{-2}	−1.41	−1.43	−1.42	−20
$W_2(PPh_2)_2$[c]	−1.44	−1.26	−1.35	+180	8.0×10^{-1}	1.4×10^{-2}	−1.46	−1.30	−1.38	+160

[a] Computed by density functional theory in acetonitrile [$Mo_2(SPh)_2$ and $W_2(SPh)_2$] or acetone [$Mo_2(PPh_2)_2$ and $W_2(PPh_2)_2$] as described in [72]
Potentials reported versus $Fc^{+/0}$ with $E_{mid}^{\circ\prime}=(E_i^{\circ\prime}+E_{ii}^{\circ\prime})/2$ and $\Delta E^{\circ\prime}=E_{ii}^{\circ\prime}-E_i^{\circ\prime}$

[b] Experimental data in 0.1 M Bu_4NBF_4/acetonitrile from [62]

[c] Experimental data in 0.3 M Bu_4NPF_6/acetone from [68]

[d] Estimated from experimental data for $W_2(SBz)_2$ derivative in 0.1 M Bu_4NBF_4/*N*,*N*-dimethylformamide from [63]

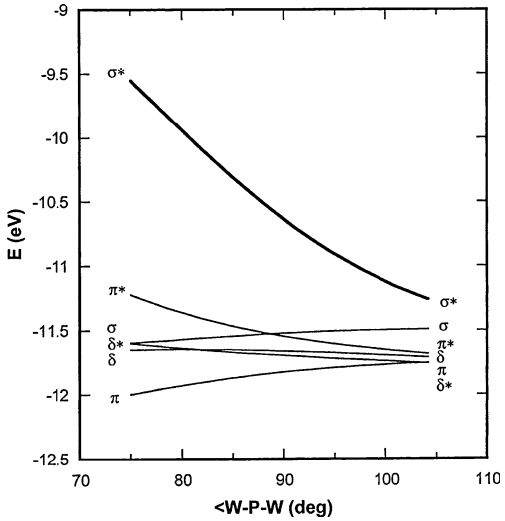

Fig. 6 Walsh diagram from extended Hückel molecular orbital calculations of the $W_2(\mu\text{-}PH_2)_2(CO)_8^{0/2-}$ redox system (reprinted with permission from [68], Copyright 2002, American Chemical Society)

bridging ligands play an important role in electron transfer energetics. (3) The results for $[Mo_2(\mu\text{-}PPh_2)_2(CO)_8]^{0/2-}$ and $[W_2(\mu\text{-}PPh_2)_2(CO)_8]^{0/2-}$ confirm that the second electrode reaction is markedly slower than the first ($k_{sh,i}>k_{sh,ii}$) and suggest that greater structural change accompanies addition of the second electron. (4) On the basis of the $k_{sh,ii}$ values, electron transfer kinetics are effectively metal-independent, but are demonstrably greater for sulfido- than for phosphido-bridged complexes. This observation is not anticipated from consideration of nuclear displacement energetics because it is predicted from bond distance/force constant correlations [68, 70] that M–S and M–P bond deformation constants should be nearly identical.

To gain a more complete understanding of structural influences on electrochemical behavior, we have carried out DFT studies on the $M_2(\mu\text{-}ER_n)_2(CO)_8$ redox systems [71, 72]. The objectives were to understand the pronounced influence of ligand rather than metal on electron transfer energetics and to understand how and why electrochemical cleavage of the metal–metal σ bond leads to the asymmetric energy distortion ($E_{ii}^{\circ\prime}>E_i^{\circ\prime}$) required for potential inversion. Computed values of $E_i^{\circ\prime}$, $E_{ii}^{\circ\prime}$, and $E_{mid}^{\circ\prime}$ are collected in Table 4, where they agree well with their experimental counterparts and replicate the observed ligand dependence and metal independence of the potentials. It is found that $E_{ii}^{\circ\prime}>E_i^{\circ\prime}$ for the W complexes, but this condition is not strictly true for Mo. However, within the error of the theoretical methodology, an apparent two-electron transfer or two irresolvable one-electron events is predicted by $\Delta E_{comp}^{\circ\prime}$ for all species.

The clearest explanation of the molecular features promoting potential inversion comes from consideration of orbital energetics. The redox-active orbital previously has been envisioned as resulting simply from a metal–metal

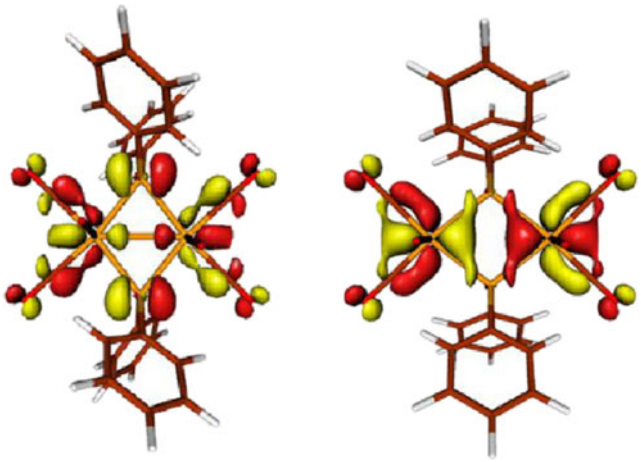

Fig. 7 Isosurface plots of the redox-active orbital of $W_2(\mu\text{-}PPh_2)_2(CO)_8$ (*left*) and $W_2(\mu\text{-}PPh_2)_2(CO)_8^{2-}$ (*right*). (Reprinted with permission from [72], Copyright 2010, American Chemical Society)

σ antibonding interaction between the $d_{x^2-y^2}$ orbital on each metal plus some in-plane CO back-bonding. However, as illustrated by the isosurface plots in Fig. 7, the redox-active orbital contains substantial bridging ligand character in the oxidized form and transitions to a primarily metal-based orbital in the reduced form. This redox non-innocence correlates with the observation that redox potentials are more representative of the identity of the bridging ligand

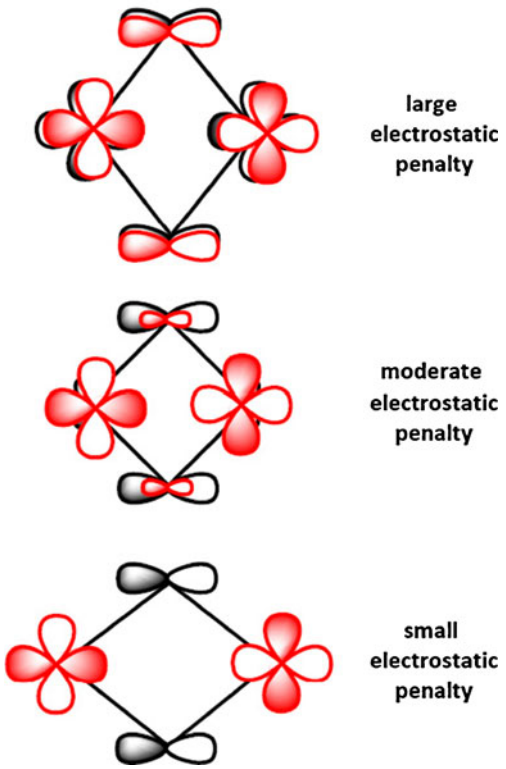

Scheme 4 Cartoon depicting overlap of in-phase (*black*) and out-of-phase (*red*) orbitals leading to disproportionate electrostatic penalties during two-electron reduction of $M_2(\mu\text{-}ER_n)_2(CO)_8$ complexes

than the metal. Metal–ligand mixing is present in all cases, but redox non-innocence is more pronounced for the phosphido-bridged species. This is true because S is more electronegative than P, which results in the bridging RS^- units having lower orbital energies that mix less effectively with those of the metal.

As electrons are added to the σ*-type redox-active orbital, its energy falls in conjunction with the geometric structural changes as shown in Fig. 6. However, the convex curvature of this energy–distance plot is not consistent with potential inversion, which requires greater stabilization of the second electron step [72, 73]. We have determined that much of the needed stabilizing increment arises from electrostatic interactions between the out-of-phase redox-active σ* LUMO and its in-phase complement, which is the HOMO-15 in $Mo_2(\mu\text{-}PPh_2)_2(CO)_8$ and the HOMO-10 in $Mo_2(\mu\text{-}SPh)_2(CO)_8$. The spatial relationship of these in-phase and out-of-phase orbitals explains much about the electrostatic interactions during two-electron transfer. As shown at the top of Scheme 4, a large electrostatic penalty is associated with the addition of one electron to the out-of-phase LUMO (red) because of spatial similarity to its in-phase complement (black). After the addition of the first electron and structural relaxation, the singly occupied redox orbital becomes more metal-based in character and more spatially confined to the M–M axis, whereas the in-phase orbital becomes more localized on the bridging ligand (Scheme 4, middle). The electrostatic interaction penalty is now reduced and its impact minimized upon the addition of the second electron, where structural relaxation leads to a virtually complete separation of the in-phase and out-of-phase orbitals (Scheme 4, bottom). We believe that the unusually unfavorable electrostatic repulsion associated with the first electron transfer and its diminished influence as reduction proceeds provides the disproportionate contribution to energetic stabilization of the second electron transfer that is required for potential inversion. Also, because greater metal–ligand mixing is found in phosphido- versus sulfido-bridged species, it is possible that the more extensive potential inversion and more sluggish electron transfer kinetics of the former complexes arise in part from these electrostatic effects.

Acknowledgment The author would like to express his thanks to the many dedicated co-workers named in the references for their contributions to this work and to the National Science Foundation and the Petroleum Research Fund of the American Chemical Society for generous financial support.

References

1. Bard AJ, Faulkner LR (2001) Electrochemical methods. Fundamentals and applications. Wiley, New York
2. Savéant JM (2006) Elements of molecular and biomolecular electrochemistry. An electrochemical approach to electron transfer chemistry. Wiley-Interscience, Hoboken
3. Kissinger PT, Heineman WR (1996) Laboratory techniques in electroanalytical chemistry, 2nd edn. Marcel Dekker, New York
4. Rudolph M, Reddy DP, Feldberg SW (1994) Anal Chem 66: A589–A600
5. Parr RG, Yang W (1989) Density functional theory of atoms and molecules. Oxford University Press, New York
6. Burgess BK, Lowe DJ (1996) Chem Rev 96:2983–3011
7. Seefeldt LC, Hoffman BM, Dean DR (2009) Annu Rev Biochem 78:701–722
8. Hille R (1996) Chem Rev 96:2757–2816
9. Enemark JH, Cooney JJA (2004) Chem Rev 104:1175–1200
10. Steifel EI (1977) Progr Inorg Chem 22:1–223
11. Schultz FA, Ott VR, Rolison DS, Bravard DC, McDonald JW, Newton WE (1978) Inorg Chem 17:1758–1765
12. Einsle O, Tezcan FA, Andrade SLA, Schmid B, Yoshida M, Howard JB, Rees DC (2002) Science 254:1696–1700
13. Hine FJ, Taylor AJ, Garner CD (2010) Coord Chem Rev 254:1570–1579
14. Olson GM, Schultz FA (1994) Inorg Chim Acta 225:1–7
15. Uhrhammer D, Schultz FA (2004) Inorg Chem 43:7389–7395
16. Chang CSJ, Collison D, Mabbs FE, Enemark JH (1990) Inorg Chem 29:2261–2267
17. Carducci MD, Brown C, Solomon EI, Enemark JH (1994) J Am Chem Soc 116:11856–11868
18. Westcott BL, Gruhn NE, Enemark JH (1998) J Am Chem Soc 120:3382–3386
19. McElhaney AE, Inscore FE, Schirlin JT, Enemark JH (2002) Inorg Chim Acta 341:85–90
20. Inscore FE, Knottenbelt SZ, Rubie ND, Joshi HK, Kirk ML, Enemark JH (2006) Inorg Chem 45:967–976
21. Nicholson RS (1965) Anal Chem 37:1351–1355
22. Marcus RA (1968) Electrochim Acta 13:995–1004
23. Weaver MJ (1976) J Phys Chem 80:2645–2651
24. Perkins PG, Schultz FA (1983) Inorg Chem 22:1133–1136
25. Pearson RG (1990) Coord Chem Rev 100:403–425
26. Inscore FE, McNaughton R, Westcott BL, Helton ME, Jones R, Dhawan IK, Enemark JH, Kirk ML (1999) Inorg Chem 38:1401–1410
27. Kennepohl P, Solomon EI (2003) Inorg Chem 42:679–688
28. Kennepohl P, Solomon EI (2003) Inorg Chem 42:689–695
29. Kennepohl P, Solomon EI (2003) Inorg Chem 42:696–708
30. Turner JW, Schultz FA (2001) Coord Chem Rev 219–221:81–97
31. Meunier B, de Visser SP, Shaik S (2004) Chem Rev 104:3947–3980
32. Shaver MP, Allan LEN, Rzepa HS, Gibson VC (2006) Angew Chem Int Ed 45:1241–1244
33. Kahn O, Martinez CJ (1998) Science 279:44–48
34. Osorio EA, Moth-Poulsen K, van der Zant HSJ, Paaske J, Hedegård P, Flensberg K, Bjørnholm T (2010) Nano Lett 10:105–110
35. Hendry P, Ludi A (1990) Adv Inorg Chem 35:117–198
36. Newton MD (1991) J Phys Chem 95:30–38
37. Shalders RD, Swaddle TW (1995) Inorg Chem 34:4815–4820
38. Crawford PW, Schultz FA (1994) Inorg Chem 33:4344–4350
39. König E (1987) Progr Inorg Chem 35:527–622
40. Turner JW, Schultz FA (1999) Inorg Chem 38:358–364
41. Turner JW, Schultz FA (2001) Inorg Chem 40:5296–5298
42. Lord RL, Schultz FA, Baik MH (2009) J Am Chem Soc 131:6189–6197
43. Baik MH, Friesner RA (2002) J Phys Chem A 106:7407–7415
44. Paulsen H, Trautwein AX (2004) Top Curr Chem 235:197–220
45. Deeth RJ, Fey N (2004) J Comput Chem 25:1840–1848
46. Remacle F, Grandjean F, Long GJ (2008) Inorg Chem 47:4005–4014

47. Jensen KP, Cirera J (2009) J Phys Chem A 113:10033–10039
48. Ye S, Neese F (2010) Inorg Chem 49:772–774
49. Deeth RJ, Anastasi AE, Wilcockson MJ (2010) J Am Chem Soc 132:6876–6877
50. Wieghardt K, Schmidt W, Herrmann W, Küppers HJ (1983) Inorg Chem 22:2953–2956
51. van Gaal HLM, van der Linden JGM (1982) Coord Chem Rev 47:41–54
52. Griffith JS (1964) The theory of transition metal ions. Cambridge University Press, Cambridge
53. Sharpe P, Eyler JR, Richardson DE (1990) Inorg Chem 29:2779–2787
54. de Alwis DCL, Schultz FA (2003) Inorg Chem 42:3616–3622
55. Yasuda H, Suga K, Aoyagui S (1978) J Electroanal Chem 86:259–270
56. Hossain F, Rigsby MA, Duncan CT, Milligan PL Jr, Lord RL, Baik MH, Schultz FA (2007) Inorg Chem 46:2596–2603
57. Buchen Th, Gütlich P (1995) Inorg Chim Acta 231:221–223
58. Turner JW, Schultz FA (2002) J Phys Chem B 106:2009–2017
59. Evans DH (2008) Chem Rev 108:2113–2144
60. Pipes DW, Meyer TJ (1984) J Am Chem Soc 106:7653–7654
61. Bradbury JR, Schultz FA (1986) Inorg Chem 25:4408–4416
62. Smith DA, Zhuang B, Newton WE, McDonald JW, Schultz FA (1987) Inorg Chem 26:2524–2531
63. Fernandes JB, Zhang LQ, Schultz FA (1991) J Electroanal Chem 297:145–161
64. Hill MG, Rosenhein LD, Mann KD, Mu XH, Schultz FA (1992) Inorg Chem 31:4108–4111
65. Shyu SG, Calligaris M, Nardin G, Wojcicki A (1987) J Am Chem Soc 109:3617–3625
66. Darensbourg DJ, Sanchez KM, Reibenspies J (1988) Inorg Chem 27:3636–3643
67. Shaik S, Hoffman R, Fisel CR, Summerville RH (1980) J Am Chem Soc 102:4555–4572
68. Uhrhammer D, Schultz FA (2002) J Phys Chem A 106:11630–11636
69. Ryan MD (1978) J Electrochem Soc 125:547–555
70. Conradson SD, Sattelberger AP, Woodruff WH (1988) J Am Chem Soc 110:1309–1311
71. Schultz FA, Lord RL, Yang X, Maik MH (2009) ACS Symposium Ser 1012:151–166
72. Lord RL, Schultz FA, Baik MH (2010) Inorg Chem 49:4611–4619
73. Baik MH, Ziegler T, Schauer CK (2000) J Am Chem Soc 122:9143–9154